# Coherent phonons in Si/SiGe superlattices

Y. Ezzahri,* S. Grauby, J. M. Rampnoux, H. Michel, G. Pernot, W. Claeys, and S. Dilhaire
*Centre de Physique Moléculaire Optique et Hertzienne, UMR CNRS 5798, Université Bordeaux 1, 351 cours de la libération, 33405 Talence cedex, France*

C. Rossignol
*Laboratoire de Mécanique Physique, UMR CNRS 5469, Université Bordeaux 1, 351 cours de la libération, 33405 Talence cedex, France*

G. Zeng and A. Shakouri
*Department of Electrical Engineering, University of California Santa Cruz, Santa Cruz, California 95064-1077, USA*
(Received 6 December 2006; revised manuscript received 26 February 2007; published 7 May 2007)

There are several classes of coherent phonons whose generation mechanisms are completely different: impulsive stimulated Raman scattering, Brillouin oscillations, and coherent longitudinal-acoustic-phonon Bragg reflection. All of these are investigated in Si/SiGe superlattices using a picosecond ultrasonics technique at room temperature. Bragg reflection for a single vibrational mode is related to gaps in the phonon-dispersion relation at the center and the boundary of the folded Brillouin zone. The two lowest minigaps are observed at 283 and 527 GHz. Theoretical calculations of phonon-dispersion relation and phonon reflection rate are given to explain experimental results.

DOI: 10.1103/PhysRevB.75.195309 PACS number(s): 68.35.Ja, 63.20.Dj, 68.65.Cd, 68.35.Iv

## I. INTRODUCTION

Periodic multilayers and superlattices (SLs) have been extensively investigated in semiconductor devices for their electronic, optical, thermal, and acoustic properties. The artificial periodicity of these structures drastically alters the bulk physical properties.[1] In addition to extensive investigation of electronic quantum states and transport properties, there have been a number of studies which explored the vibrational characteristics of SLs.[2] Vibrational properties of periodic multilayers and SLs have been investigated as a possible mechanism that could reduce thermal conductivity of such structures.[3] The vibrational modes of periodic multilayers are theoretically described by the superlattice dispersion curve which exhibits folding of the phonon branches into a mini-Brillouin-zone (mini-BZ) of dimension $\pi/D$, where $D$ is the period of the structure.[4] One of the most fundamental acoustic properties of a SL is the Bragg reflection of long-wavelength phonons. The Bragg condition requires $2D\cos(\theta)=n\lambda$, where $\theta$ is the angle of incidence of the phonon wave vector measured from the normal of the interfaces, $\lambda$ is the phonon wavelength, and $n$ is an integer.[2] Each phonon satisfying this condition is Bragg reflected and cannot propagate through the SL. This is analogous to electronic energy gaps; band gaps in the phonon-dispersion relation are formed at the center and at the boundary of the folded mini-BZ as a direct consequence of the Bragg reflection process.

Since the first works of Narayanamurti *et al.*[5] and Colvard *et al.*,[6] the acoustic properties of SLs have been widely studied using Raman scattering and phonon transmission spectroscopy.[2,5–13] A considerable amount of literature has been published on the acoustic properties of semiconductor superlattices and the majority of works have been concentrated on GaAs/AlAs and GaAs/$Al_xGa_{(1-x)}$As superlattices.[1] These materials were chosen because they are easy to grow and lattice matched. The acoustic impedances of different layers are quite similar.

In recent years, a number of experiments have been reported, in which coherent phonons have been generated in semiconductor structures using ultrafast laser pulses.[4,14–24] It has been shown that coherent zone folded longitudinal-acoustic phonons are excited when a femtosecond laser pulse is absorbed by the SL. The excitation process has been attributed to impulsive stimulated Raman scattering, in which the formation of an electron-hole pair is accompanied by the creation of a longitudinal-acoustic phonon.

In this paper, the picosecond ultrasonics (PU) technique is used to characterize vibrational characteristics of Si/SiGe SLs at room temperature. Several classes of coherent phonons are observed as having distinct generation mechanisms: impulsive stimulated Raman scattering (ISRS), Brillouin oscillation, and coherent longitudinal-acoustic-phonon Bragg reflection. Recently, Si/$Si_xGe_{(1-x)}$ SLs have received considerable attention. This is mainly due to the achievement of high-quality pseudomorphic growth of multilayer structures by silicon molecular-beam epitaxy.[25,26] The modified electrical and thermal properties of these structures are promising for the design of novel electronic, optoelectronic, and thermoelectric devices based on Si/$Si_xG_{(1-x)}$ SLs.[26]

The paper is organized as follows: in Sec. II, we first present the PU experimental setup and describe the sample structure. In Sec. III, we revisit the theory of folded acoustic phonons and use the Rytov elastic model to calculate both phonon-dispersion relation and phonon reflection rate.[27] Finally, in Sec. IV, we compare the experimental results with the theoretical calculations.

## II. SAMPLE DESCRIPTION AND EXPERIMENTAL SETUP

The structure studied in this work is a 3 $\mu$m Si/$Si_{0.4}Ge_{0.6}$ SL, grown on top of a 1.6-$\mu$m-thick buffer layer on a silicon

 

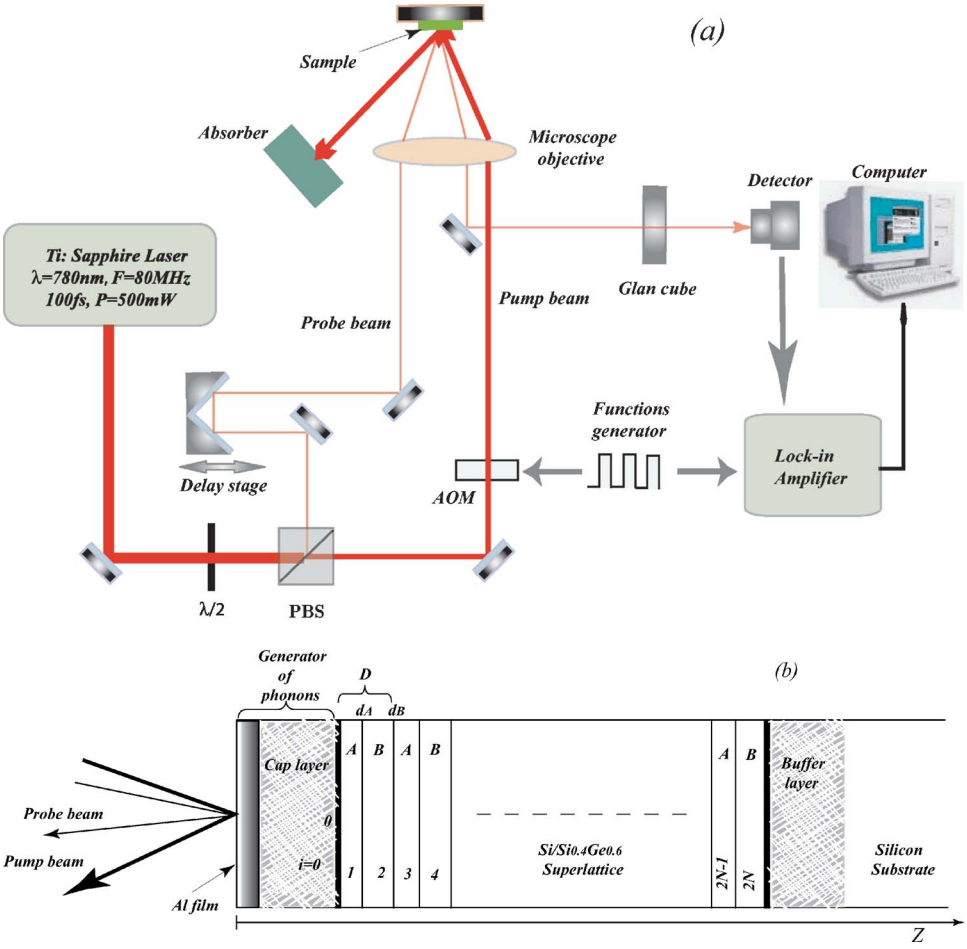


FIG. 1. (Color online) Schematic diagram of (a) the experimental setup and (b) the studied superlattice structure.

substrate which is approximately 500 $\mu$m. The buffer layer is needed to reduce mechanical stress between the substrate and the active SL caused by the lattice mismatch between Si and $Si_{0.4}Ge_{0.6}$, which is about 4.2%.[26] The buffer layer was graded in order to achieve a strain-balanced SL. On top of the SL, a 165-nm-thick $Si_{0.8}Ge_{0.2}$ cap layer was grown. Finally, a 15-nm-thick Al film was deposited on the surface using electron-beam evaporation. Figures 1(a) and 1(b) show schematic diagrams of the experimental setup and the sample, respectively.

A pulsed laser beam from a 80 MHz Ti:sapphire laser with a pulse duration of 100 fs at $\lambda=780$ nm is separated into two beams with an intensity ratio of 10:1 by a polarizing beam splitter combined to a zero order $\lambda/2$ plate. The intense "pump" beam is used to heat the metallic film, while the weaker "probe" beam is used to monitor the reflectivity variation of the film surface. The pump beam passes through an acousto-optic modulator that creates a pulse train modulated at a frequency of 700 kHz. The pump beam is focused to $\sim$20 $\mu$m. The probe beam is reflected off a retroreflector mounted on a mechanical translation stage to increase the optical path length of the probe beam and hence to modify the time delay between the pump and the probe pulses. The probe, which is centered in the heated area created by the pump pulse, is focused to $\sim$6 $\mu$m at near normal incidence. A polarizer, oriented in such a way that only the probe beam can cross it, is positioned before the photodiode which monitors the probe beam reflection off the sample. To improve the signal-to-noise ratio, the detector response at 700 kHz is then monitored by a lock-in amplifier.

## III. THEORY

### A. Longitudinal-acoustic-phonon dispersion relation

In these calculations, we focus on phonons propagating perpendicular to the SL interfaces. Phonons are considered in normal incidence with respect to the SL interface. In this case, $\theta=0$, and the Bragg reflection condition becomes $2D=n\lambda$. The basic reciprocal vector of the SL is defined by $G_0=2\pi/D$, and an equivalent form of Bragg reflection condition is

$$2Q = nG_0, \tag{1}$$

where $Q=2\pi/\lambda$ is the phonon wave vector in the SL, which describes the modulation of waves in the SL as a whole.

The interfaces of the SL are assumed to be mirror-symmetry planes of the crystal, and therefore all three modes of phonons are decoupled from each other for normal propagation.[2] The dispersion relation of folded acoustic modes in a SL made of stacking of two layers of different materials with abrupt interfaces, including the splitting at the center and the boundary of the mini-BZ, can be easily calculated in the so-called *elastic limit*, which corresponds to the frequency range in which the dispersion relations of the constituents can be assumed to be linear.[1] The exact well-

known solution is given by Rytov,[27] and is considered as the elastic version of the electronic Kronig-Penney model, in which the mass modulation along the growth direction can be considered as the counterpart of the periodic electrical potential. Afterward, we use the analogy with the electromagnetic wave propagation in a stratified media to calculate the phonon-dispersion relation of the SL using the transfer-matrix method.

The SL structure is described in Fig. 1(b). First, we consider the SL consisting of an infinite repetition of alternating layers of material $A$ with thickness $d_A$ and material $B$ with thickness $d_B$; thus, the SL period is $D=d_A+d_B$. The interfaces are parallel to the $(x,y)$ plane and the $z$ axis (growth axis) is normal to the interfaces. The equation of motion for propagation along the growth axis $z$ of longitudinal elastic waves in each layer of the SL is given by

$$\rho_i \frac{\partial^2 U_i}{\partial t^2} = \frac{\partial \sigma_i}{\partial z}. \tag{2}$$

$U_i$ and $\sigma_i$ are the displacement and the stress of a given acoustic mode, respectively, in each SL layer $i=A$, $B$. $\sigma_i = C_i(\partial U_i/\partial z)$, where $C_i$ is the $z$ component of the elastic constant tensor in layer $i$. The solution of Eq. (2) can be put in the form

$$U_i(z,t) = (a_i e^{jq_i z} + b_i e^{-jq_i z}) e^{-j\omega t}, \tag{3}$$

where $a_i$ and $b_i$ are the amplitudes of the transmitted ($+z$ propagating) and the reflected ($-z$ propagating) waves, respectively. $q_i=\omega/\nu_i$, where $\nu_i$ is the sound velocity in layer $i$. The time dependence $e^{-j\omega t}$ of $U_i$ will be removed in the subsequent analysis to simplify the notation.

$U_i$ and $\sigma_i$ must satisfy the continuity condition at the boundaries:

$$U_{A,B}|_{z=d_A,d_B} = U_{B,A}|_{z=0,0},$$

$$\sigma_{A,B}|_{z=d_A,d_B} = \sigma_{B,A}|_{z=0,0}. \tag{4}$$

At this stage, it is convenient to introduce a $2\times 2$ matrix defined by

$$M_i = \begin{pmatrix} e^{jq_i d_i} & e^{-jq_i d_i} \\ C_i q_i e^{jq_i d_i} & -C_i q_i e^{-jq_i d_i} \end{pmatrix}. \tag{5}$$

It results from Eqs. (3) and (4) that

$$\begin{pmatrix} a_A \\ b_A \end{pmatrix} = P_A \tau_{A,B} P_B \tau_{B,A} \begin{pmatrix} a_{A+1} \\ b_{A+1} \end{pmatrix}, \tag{6}$$

where $P_{A,B}$ and $\tau_{\substack{A,B\\B,A}}$ represent, respectively, the layer and interface acoustic matrices, given by

$$P_{A,B} = \begin{pmatrix} e^{-jq_{A,B}d_{A,B}} & 0 \\ 0 & e^{jq_{A,B}d_{A,B}} \end{pmatrix}$$

and

$$\tau_{\substack{A,B\\B,A}} = \frac{1}{t_{\substack{A,B\\B,A}}} \begin{pmatrix} 1 & r_{\substack{A,B\\B,A}} \\ r_{\substack{A,B\\B,A}} & 1 \end{pmatrix}. \tag{7}$$

$t_{\substack{A,B\\B,A}}$ and $r_{\substack{A,B\\B,A}}$ are, respectively, the transmission and reflection coefficients of longitudinal-acoustic phonons at normal incidence at the interfaces $A/B$ and $B/A$. They are defined by

$$t_{\substack{A,B\\B,A}} = \frac{2Z_{A,B}}{Z_A + Z_B} \quad \text{and} \quad r_{\substack{A,B\\B,A}} = \frac{Z_{A,B} - Z_{B,A}}{Z_A + Z_B}, \tag{8}$$

where $Z_i=\rho_i \nu_i$ is the acoustic impedance of layer $i$.

The acoustic transfer matrix of the SL is defined by $T_{ac} = P_A \tau_{A,B} P_B \tau_{B,A}$. $\mathrm{Det}(T_{ac})=1$, which means that $T_{ac}$ is an orthogonal matrix, and hence the eigenvalues of $T_{ac}$ must be expressible in the form $(e^{j\theta}, e^{-j\theta})$. Then, it is natural to define the SL wave number $Q$ by the relation[14]

$$\theta = QD. \tag{9}$$

The phonon-dispersion relation of the SL is then given by

$$\cos(QD) = \frac{1}{2}\mathrm{Tr}(T_{ac}) = \cos(q_A d_A)\cos(q_B d_B) - \frac{1 - r_{A,B} r_{B,A}}{t_{A,B} t_{B,A}} \sin(q_A d_A)\sin(q_B d_B). \tag{10}$$

We should note here that we find exactly the well-known Rytov relation.[27] In fact,

$$\frac{1 - r_{A,B} r_{B,A}}{t_{A,B} t_{B,A}} = \frac{1 + \delta^2}{2\delta}. \tag{11}$$

$\delta=Z_A/Z_B$ is the ratio of the acoustic impedances of the first and the second layer of the SL, respectively.

The right side of Eq. (10) is a continuous function of $\omega$, and its modulus exceeds unity for some ranges of $\omega$. On the other hand, the modulus of the left side is bounded by 1. Therefore, frequency gaps exist for the general $\omega$-versus-$q$ relation.[2,7] These gaps occur for $Q=n\pi/D$, which is exactly the Bragg reflection condition at normal incidence [Eq. (1)]. Several authors have investigated in detail the frequency gaps at the center and the boundary of the mini-BZ.[2,4] The frequencies at the center and the boundary of the mini-BZ and the width of the frequency gaps may be derived from a simple perturbation calculation as was pointed out by Tamura *et al.*[2] In this case, it is more convenient to write Eq. (10) in the form

$$\cos(QD) = \cos(q_A d_A + q_B d_B) - \gamma \sin(q_A d_A)\sin(q_B d_B), \tag{12}$$

where $\gamma=(1-\delta)^2/2\delta$. For most SL, $\delta$ is close to unity, and the second term of Eq. (12) can be regarded as a small perturbation. Then, for normal incidence the center of the $p$th-order frequency gap is given by

$$\omega_p = p\frac{\pi v_{eff}}{D}. \tag{13}$$

The integer $p$ is even at the center of the mini-BZ, and odd at the boundary. $\nu_{eff}$ is the effective sound velocity in the SL given by

$$\frac{D}{\nu_{eff}} = \frac{d_A}{\nu_A} + \frac{d_B}{\nu_B}. \tag{14}$$

The latter equation simply means that the transit time through a period is the sum of the transit times through each layer.

Using a similar method, the widths of the frequency gaps are given by

$$\Delta\omega_p = 2\frac{\nu_{eff}}{D}\left|\chi \sin\left[\frac{p\pi}{2}\frac{d_A/\nu_A - d_B/\nu_B}{d_A/\nu_A + d_B/\nu_B}\right]\right|$$

at the mini-BZ center, and $p$ is even,

$$\Delta\omega_p = 2\frac{\nu_{eff}}{D}\left|\chi \cos\left[\frac{p\pi}{2}\frac{d_A/\nu_A - d_B/\nu_B}{d_A/\nu_A + d_B/\nu_B}\right]\right|$$

at the mini-BZ boundary, and $p$ is odd. (15)

From Eq. (15), we can see that the width of the frequency gap is proportional to the acoustic modulation $\chi=(Z_A-Z_B)/\sqrt{Z_AZ_B}$ and inversely proportional to the SL period thickness $D$.[4] We should note here that for our studied $Si/Si_{0.4}Ge_{0.6}$ SL, $\delta\approx 1.25$ and $\chi\approx 0.23$. The acoustic impedance of $Si_{0.4}Ge_{0.6}$ is estimated using average values of density and sound velocity of Si and Ge. The center of the first two order frequency gaps are then given, respectively, by $\omega_1\approx 270$ GHz and $\omega_2\approx 540$ GHz, and their corresponding widths are given, respectively, by $\Delta\omega_1\approx 29$ GHz and $\Delta\omega_2\approx 40$ GHz. The values of $\omega_1$ and $\omega_2$ are in very good agreement with the observed experimental frequencies, as we will see in Sec. IV.

At the limit $\omega\to 0$, the phonon wavelength becomes much longer than the SL periodicity, becoming a bulk sound wave with a linear dispersion relation given by[2,7]

$$\nu_{SL} = \frac{\omega}{Q} = D\left[\left(\frac{d_A}{\nu_A}\right)^2 + \left(\frac{d_B}{\nu_B}\right)^2 + \frac{1+\delta^2}{\delta}\frac{d_Ad_B}{\nu_A\nu_B}\right]^{-1/2}. \tag{16}$$

This is exactly the same formula given the sound velocity of the SL considered as an effective acoustic media.[28]

Now, after the discussion about the dispersion relation, let us examine the acoustic-phonon reflection rate.

### B. Longitudinal-acoustic-phonon reflection rate

The reflection rate of phonons propagating along the growth direction $z$ in a finite SL is calculated following the method proposed by Tamura *et al.* to calculate the transmission rate of phonons.[2] In this situation, phonons of a given mode are incident from the phonon generator (the metallic film+cap layer) toward $N$ periods of the SL, as illustrated in Fig. 1(b). All phonons which satisfy Bragg reflection condition are reflected off the SL and cannot propagate through it.

To calculate the SL phonon reflection rate, we began by calculating the entire SL acoustic transfer matrix which is given by $T_{ac}^{SL}=[T_{ac}]^N$. Fortunately, this is possible analytically using the well-known Cailey-Hamilton theorem: If $M$ is a $2\times 2$ matrix which has two distinct eigenvalues $\lambda_1$ and $\lambda_2$, the $N$ power of the matrix $M$ is then obtained by

$$M^N = \frac{\lambda_1^N - \lambda_2^N}{\lambda_1 - \lambda_2}M - \lambda_1\lambda_2\frac{\lambda_1^{N-1} - \lambda_2^{N-1}}{\lambda_1 - \lambda_2}I. \tag{17}$$

$I$ is the $2\times 2$ identity matrix. The next step is to relate the vector $\begin{pmatrix} a_{CL} \\ b_{CL}\end{pmatrix}$ into the cap layer to the vector $\begin{pmatrix} a_{su} \\ b_{su}\end{pmatrix}$ into the substrate. The substrate is considered to be a semi-infinite medium, and then $b_{su}=0$. After some easy algebra, we find that

$$\begin{pmatrix} a_{CL} \\ b_{CL}\end{pmatrix} = \tau_{CL,A}T_{ac}^{SL}\tau_{A,su}\begin{pmatrix} a_{su} \\ 0\end{pmatrix}, \tag{18}$$

where $\tau_{CL,A}$ and $\tau_{A,su}$ are the acoustic transfer matrices of the cap layer/first SL layer $A$ interface and that of the SL layer $A$/substrate interface, respectively. These are given by

$$\tau_{CL,A} = \frac{1}{t_{CL,A}}\begin{pmatrix} 1 & r_{CL,A} \\ r_{CL,A} & 1\end{pmatrix} \quad \text{and} \quad \tau_{A,su} = \frac{1}{t_{A,su}}\begin{pmatrix} 1 & r_{A,su} \\ r_{A,su} & 1\end{pmatrix}. \tag{19}$$

The solution of Eq. (18) yields the amplitude $b_{CL}$ of the reflected wave in the cap layer and the amplitude $a_{su}$ of the transmitted wave in the substrate.

The reflection rate is defined as the energy flux of the phonons reflected off the SL normalized by the energy flux of the incident wave in the cap layer. The energy flux is given by[2]

$$\Phi_i = \frac{1}{2}\rho_i\omega^2V_i|a_i|^2. \tag{20}$$

$V_i$ is the group velocity of the acoustic wave. For normal incidence and in the continuum approximation, we can take $V_i=\nu_i$.[2]

From Eqs. (18) and (20), we can get the expression of the reflection rate of phonons as

$$\Xi = \frac{\Phi_{CL,b}}{\Phi_{CL,a}} = \left|\frac{(\tau_{CL,A}T_{ac}^{SL}\tau_{A,su})_{21}}{(\tau_{CL,A}T_{ac}^{SL}\tau_{A,su})_{11}}\right|^2. \tag{21}$$

$(\tau_{CL,A}T_{ac}^{SL}\tau_{A,su})_{21}$ and $(\tau_{CL,A}T_{ac}^{SL}\tau_{A,su})_{11}$ are, respectively, the (2,1) and the (1,1) element of the matrix $\tau_{CL,A}T_{ac}^{SL}\tau_{A,su}$. In Figs. 2(a) and 2(b), we presented the calculated reflection rate for longitudinal-acoustic phonons propagating from a $Si_{0.8}Ge_{0.2}$ cap layer through a $Si/Si_{0.4}Ge_{0.6}$ 20 periods and the corresponding phonon-dispersion relation, respectively. In this calculation, we have used the data concerning the SL structure studied experimentally, except for the number of periods which is in reality 246, and $d_A=2d_B=8$ nm. In fact, within 20 periods the reflectivity coefficient reaches already 99% at both the center and the edge of the mini-BZ, and using a higher number of periods this value slowly increases up to the perfect value of 100%. In Fig. 2(b), we show the dispersion relation for both configurations $(A/B/A/B/\ldots)$

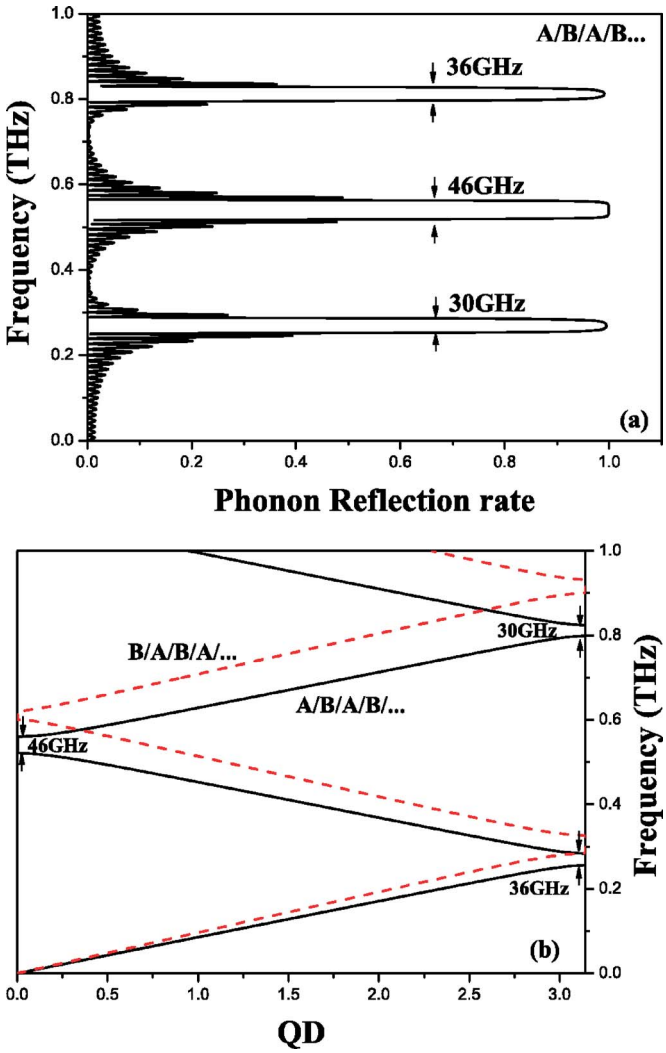


FIG. 2. (Color online) (a) Calculated phonon reflection rate for an $A/B/A/B\ldots$ configuration of the SL, and (b) phonon-dispersion relation for both $A/B/A/B\ldots$ and $B/A/B/A\ldots$ configurations of the SL, with $A \equiv Si_{0.4}Ge_{0.6}$ and $B \equiv Si$.

and $(B/A/B/A/\ldots)$, with $A=Si_{0.4}Ge_{0.6}$ and $B=Si$. The comparison with experiment will allow us to identify the first layer of the SL and its exact configuration. Table I recapitulates all geometrical and physical properties of the entire

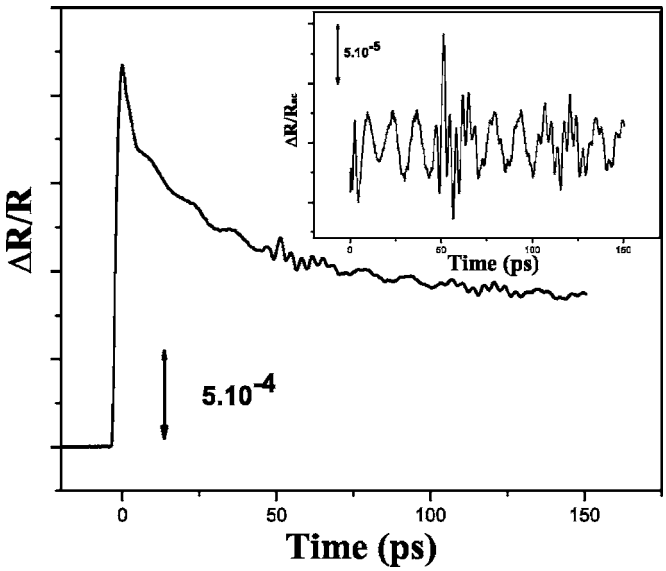


FIG. 3. Experimental reflectivity relative change as a function of time delay; the inset shows the acoustic contribution to the signal after subtraction of the thermal background.

structure: Al film, cap layer, SL, and the substrate used in the simulations.

Figure 2(a) reveals the same characteristics as the transmission rate curves,[2,5,8] except that we have peaks instead of dips. The same correlations between the width of the frequency gaps and the magnitude of the reflection peaks can be seen. Increasing the number of the SL periods increases the magnitude of the reflection peaks as well as the number of small oscillations. Additional oscillations can be understood as resulting from interferences between reflected and transmitted phonon waves.

## IV. EXPERIMENTAL RESULTS AND DISCUSSION

### A. Whole acoustic contribution

Figure 3 shows the relative change in the SL sample reflectivity as a function of the time delay. Room-temperature measurements were performed using PU at a wavelength of 780 nm. The inset shows the acoustic contribution to the signal after subtraction of the thermal background.

TABLE I. Geometrical and physical properties of the Al layer, the $Si_{0.8}Ge_{0.2}$ cap layer, the $Si/Si_{0.4}Ge_{0.6}$ superlattice, and the substrate used in the simulations.

| Layer | Thickness (nm) | Density ($kg/m^3$) | Sound velocity (m/s) | Refraction coefficient $n'$ at $\lambda=800$ nm | Extinction coefficient $n''$ at $\lambda=800$ nm |
|---|---|---|---|---|---|
| Al | 15 | 2700 | 6422 | 2.685 | 2.699 |
| $Si_{0.8}Ge_{0.2}$ cap layer | 165 | 3007 | 7262 | 3.76 | 0.0099 |
| $Si_{0.4}Ge_{0.6}$ ($A$) | 8 | 4245 | 5818 | 4.07 | 0.028 |
| Si ($B$) | 4 | 2329 | 8427 | 3.69 | 0.0065 |
| Si substrate | ~500 000 | 2329 | 8427 | 3.69 | 0.0065 |

A modeling program was used to analyze the acoustic data. Details of the model are described in Refs. 28 and 29. Rigorous physical models for both the optical and acoustical properties of the samples are used for this simulation. First, the deposited heat is calculated using the optical constants in each layer of the structure. From this heat distribution, the initial photothermal stress in the whole multilayer is determined. Then, the acoustic field in all layers of the sample is determined in the frequency domain. Finally, time-dependent amplitude and phase perturbations of the laser pulse probe reflection induced by the elastic field are calculated by fast inverse Fourier transform. Acoustic attenuation, adhesion, and roughness of the interfaces have also been considered in this model. This simulation program is easy to use and provides very fast results (about 10 s on a personal computer).

In the experiments described here, the pump beam was focused onto a spot having a diameter of roughly 20 $\mu$m, which is much larger than the whole explored depth inside the multilayer structure. Consequently, a one-dimensional model (along the stacking direction $z$) can be used to describe both the elastic wave generation and the detection processes; only longitudinal waves have to be considered,[30] as we have seen in Sec. III.

The relative change in reflectivity was calculated in a previous article[31] and the main results are reviewed here. The structure is modeled as $2N$ layers indexed by $i$, with the cap layer corresponding to $i=0$ and the substrate to $i=2N+1$. $d_i$ is the thickness of the layer $i$. A local coordinate $z$, defined within each layer, runs from 0 to $d_i$. The electromagnetic field in layer $i$ can be written as the sum of two counter propagating plane waves:

$$E_i(z) = \alpha_i e^{jk_i z} + \beta_i e^{-jk_i z}, \tag{22}$$

where $k_i = \sqrt{\varepsilon_i} k_0$, $\varepsilon_i$ is the dielectric constant, and $k_0$ is the optical wave vector in vacuum. The reflection coefficient $R_0 = \beta_0 / \alpha_0$ of the entire structure can be related to the amplitudes $(\alpha_i, \beta_i)$ of the forward and backward electromagnetic fields. These can be calculated using transfer-matrix formalism. The probe pulse is affected by the acoustic field propagating within a layer in two ways: on the one hand, each interface is displaced by the acoustic wave; on the other hand, the dielectric constant is modified by the elastic strain $\eta$. The relative change of reflectivity is thus the sum of these two contributions and it can be written as

$$\frac{\Delta R}{R_0}(t) = \frac{jk_0}{n_0 \alpha_0 \beta_0} \sum_{i=0}^{2N+1} \left\{ 2\varepsilon_i \alpha_i \beta_i [U_i(t) - U_{i-1}(t)] + \frac{1}{2} \frac{\partial \varepsilon_i}{\partial \eta} \int_0^{d_i} dz\, \eta_i(z,t) [\alpha_i e^{jk_i z} + \beta_i e^{-jk_i z}]^2 \right\}, \tag{23}$$

with $d_{2N+1} \to +\infty$ and $U_{-1}(t) = 0$; $\partial \varepsilon_i / \partial \eta$ and $U_i$ are the photoelastic coefficient and the normal acoustic displacement in the layer $i$, respectively. The relative change in reflectivity is a complex quantity which can be expressed as $\Delta R(t)/R_0 = P(t) + j\Phi(t)$. Since $10^{-7} \leqslant \Delta R(t)/R_0 \leqslant 10^{-5}$, $P(t)$ and $\Phi(t)$ stand for the relative change in the amplitude and in the phase of the reflected electromagnetic beam, respectively.

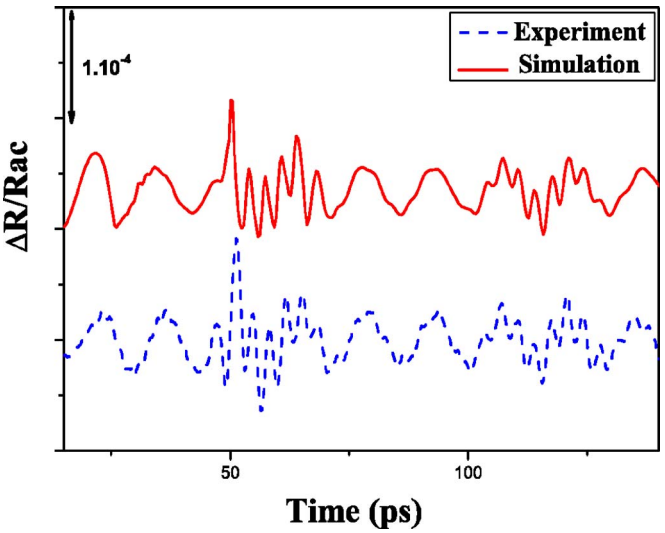


FIG. 4. (Color online) Comparison between experimental (dashed line) and theoretical (solid line) relative changes in reflectivity for the acoustic signal in the inset of Fig. 3.

Both the real and the imaginary parts, $P(t)$ and $\Phi(t)$, can be obtained through interferometric detection.[32]

To use Eq. (23), the acoustic fields, namely, $U_i(t)$ and $\eta_i(z,t)$, must be determined within each layer. This is a complex task since each individual layer acts as an acoustic source as far as the pump beam penetrates in the structure, and the fields generated by these many sources propagate and superimpose. The problem can be solved in the frequency domain expanding the acoustic field in terms of stationary waves within each layer as we have seen in Sec. III:

$$U_i(z,\omega) = a_i e^{jq_i z} + b_i e^{-jq_i z}, \tag{24}$$

where $a_i$ and $b_i$ are the complex amplitudes of counterpropagating acoustic waves in the layer $i$ and $q_i = \omega / v_i$ is the acoustic wave vector. As we have seen in detail in Sec. III, using transfer-matrix formalism, $a_i$ and $b_i$ can be expressed in terms of $a_{i-1}$ and $b_{i-1}$ and also as a function of the acoustic source in the layer $i$ due to the absorption of the pump pulse. We have performed numerical simulations according to this scheme and the results will be described later on.

The problem of acoustic propagation in multilayers when the acoustic sources are neglected is much simpler and the main results were given in Sec. III.

We have plotted in Fig. 4 the real part of the simulated relative change in reflectivity of the studied sample including the Al film, the cap layer, the $Si/Si_{0.4}Ge_{0.6}$ SL, and the Si substrate, in comparison with the experimental acoustic contribution (inset of Fig. 3). The thermal background was subtracted in order to allow comparison with numerical simulations. The relative change in reflectivity, calculated using the values in Table I, perfectly fits our experimental data. Only 20 periods were used in the calculations. Including the additional layers only increases the computational time without affecting the physical conclusions.

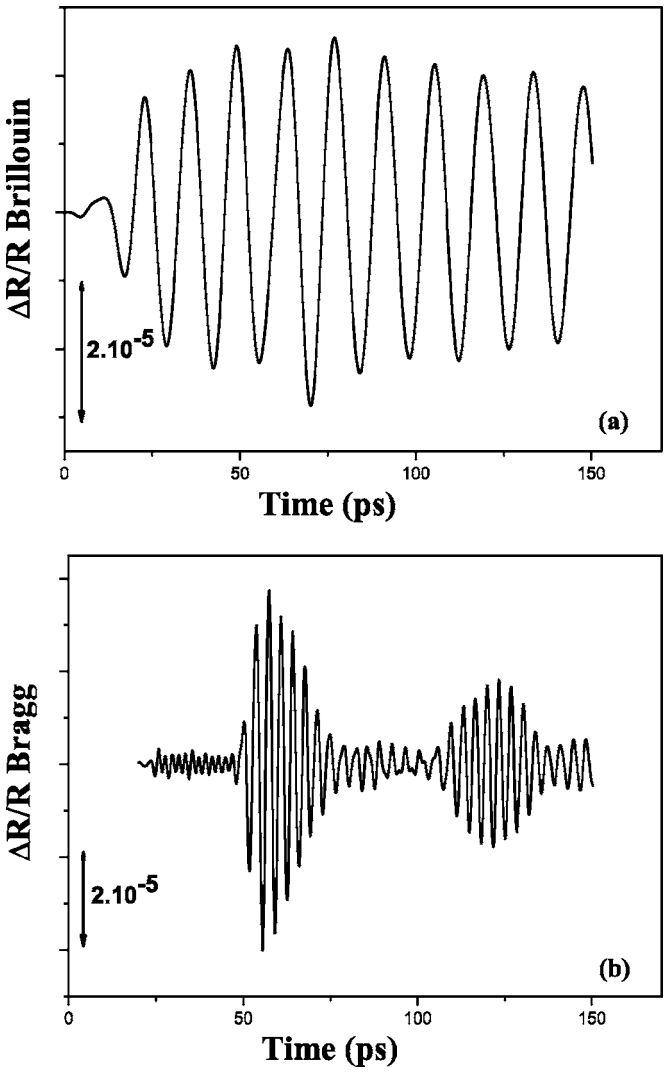


FIG. 5. (a) Brillouin oscillation and (b) Bragg reflection oscillation after Bessel numerical filtering of the curve in the inset of Fig. 3.

### B. Oscillation types and their origins

As we can see in the inset of Fig. 3, in the acoustic contribution three essential oscillations are clearly shown: a slow oscillation and two fast oscillations. In order to separate them, a Bessel bandpass numerical filter was used; the high and low frequencies of the filter were varied to distinguish each type of oscillation. The result is shown in Figs. 5(a) and 5(b).

#### *1. Brillouin oscillation*

The optical penetration length of the Al film at the wavelength of the experiment is about 7 nm, and almost 80% of the pump-laser pulse energy is absorbed within the Al film. The remaining 20% reaches the $Si_{0.8}Ge_{0.2}$ cap layer directly. In the metal layer, light is first absorbed by electrons; these electrons then transfer their excess energy to the lattice through electron-phonon collisions. They may diffuse along a significant distance before they lose all their energy, but ultimately remain confined in the metal layer due to the Schottky barrier. The energy gap of the cap layer is $E_g \approx 1.04$ eV at room temperature (300 K).[33] The optical properties of the SL should be close to those of the cap. The pump pulse at $\lambda = 780$ nm has energy of $E_p \approx 1.59$ eV. Not only is the pump light absorbed by the cap layer, it also reaches the SL structure and then produces electrons and holes in both structures. These electrons and holes relax to the band edge by emission of phonons of energy $E_p - E_g$. In the metal film and in both semiconductor structures (the cap layer and the SL), absorption of the pump-laser pulse generates a *coherent acoustic-phonon wave packet* (acoustic strain field) that propagates through the sample and causes a spatiotemporal modulation in the dielectric constant. This change is responsible for the first oscillating behavior seen in the probe field reflectivity signal and confirmed with numerical simulation (Fig. 4). This type of slow oscillation is called the *Brillouin oscillation*. Oscillations result from the interference between the probe beam reflected off the moving strain pulse and the incident probe beam.[34] The idea of the Brillouin oscillation can be well captured by forming an analogy to a Fabry-Pérot cavity with a variable length; the cavity would be formed by the moving acoustic strain pulse and the sample free surface. A good analysis of this type of oscillations is given by Liu *et al.*[22] It was shown that carrier generation is essential in observing these oscillations and both amplitude and period of these oscillations are strong functions of the laser probe energy and the thickness of the semiconductor sample.[22] Since the optical and acoustical properties of the cap layer and the SL structure, considered as an effective medium, are quite similar, there is no change in the observed Brillouin oscillation. We can affirm, however, that the major contribution comes from the cap layer, as it is the first semitransparent layer where light enters. In the case of normal incidence, which is our case, the frequency of the Brillouin oscillation is given by $f_{Brillouin} = 2\nu_{CL} n_{CL}/\lambda$,[30] where $\upsilon_{CL}$ and $n_{CL}$ are the longitudinal-acoustic sound velocity and the index of refraction of the cap layer, respectively, and $\lambda$ is the probe beam wavelength. The measured frequency of Brillouin oscillation is $f_{Brillouin} \approx 73$ GHz. The combination of this value with the value of the wavelength of the probe beam $\lambda = 780$ nm, and the estimated value of the longitudinal-acoustic sound velocity of the cap layer $\nu_{CL} \approx 7262$ m/s,[28] gives the value of the index of refraction of the cap layer $Si_{0.8}Ge_{0.2}$ at the wavelength of the experiment; we find $n_{CL} \approx 3.92$. This value is quite comparable to values of index of refraction of semiconductors at this wavelength and at room temperature.[35]

#### *2. Phonon Bragg reflection*

As mentioned in the Introduction, the artificial periodicity of SLs allows them to behave like an interference frequency filter for phonons.[5] In fact, at normal incidence, each phonon whose wave vector satisfies the Bragg condition [Eq. (1)] will be reflected off the SL and will be unable to propagate through it.

In the experiment, the coherent acoustic-phonon wave packet generated within the metal film can be considered to be produced without thermal diffusion since the temperature distribution in the metal film is uniform. Hence, in the ap-

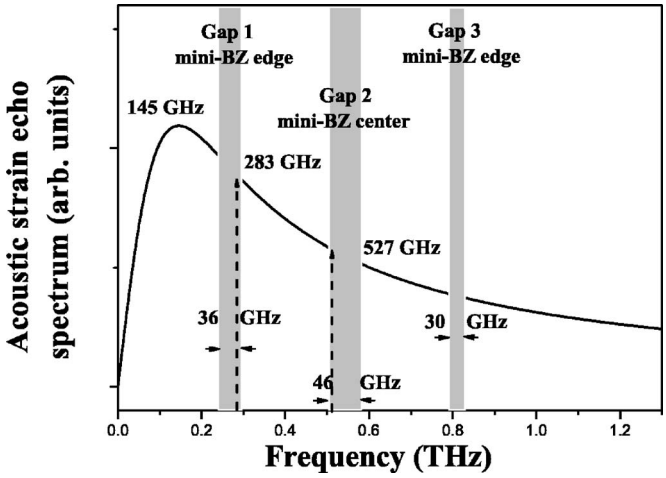


FIG. 6. Modulus of the spectrum of the acoustic strain field generated in semi-infinite Al film; the hatched bands indicate the frequency gaps in the dispersion relation of the superlattice.

proximation of semi-infinite medium in the growth direction ($z$ axis), the Fourier transform of the acoustical deformation $\eta_{33}$ is proportional to $2\pi f/[4\pi^2 f^2+(\nu_{\mathrm{Al}}/\xi_{\mathrm{Al}})^2]$,[36] which has a maximum for a frequency $f=\nu_{\mathrm{Al}}/2\pi\xi_{\mathrm{Al}}$, where $\nu_{\mathrm{Al}}$ and $\xi_{\mathrm{Al}}$ are the sound velocity and the optical penetration length of the Al film, respectively. As we can see in Fig. 6, the spectrum exhibits a maximum at $f\approx 145$ GHz and has components extending up to about 1 THz. On the other hand, as demonstrated by Thomsen *et al.*,[30] due to thermal diffusion within the semiconductor cap layer, the acoustic pulse exhibits a temporal broadening; as a consequence, the spectrum of the coherent acoustic-phonon wave packet generated within the cap layer is narrow. The association of both spectra gives a large coherent acoustic-phonon wave-packet spectrum, within which some frequencies are forbidden for propagation through the SL as qualitatively illustrated by the three hatched bands on the curve of Fig. 6. We note here that only the first two bands are observed experimentally. The phonons corresponding to these frequencies are then reflected back in the cap layer. For each frequency gap, the SL behaves like a band stop filter; in other words, the SL can be considered as a sum of many band stop filters.

Figure 7(a) shows the measured oscillations due to the reflected phonons at the $Si/Si_{0.4}Ge_{0.6}$ SL after separation from the Brillouin oscillation. A direct fast Fourier transform (FFT) of the temporal response in the dashed square yields the spectrum modulus shown in Fig. 7(b), where we can see some fringes, a consequence of the spectral interferences, with an average frequency step of about 15 GHz. The inverse of this frequency step is equivalent to the flight time between the middle of both acoustic bursts (coherent acoustic phonons), as shown in Fig. 7(a).

To get good frequency information, we make FFT of both acoustic bursts separately (solid and dotted squares); the spectra modulus are shown in Fig. 7(c), where a perfect superposition is obtained, which means that the two acoustic bursts correspond, in fact, to two successive coherent acoustic-phonon reflections. The flight time between them is the time necessary for the coherent zone folded longitudinal-

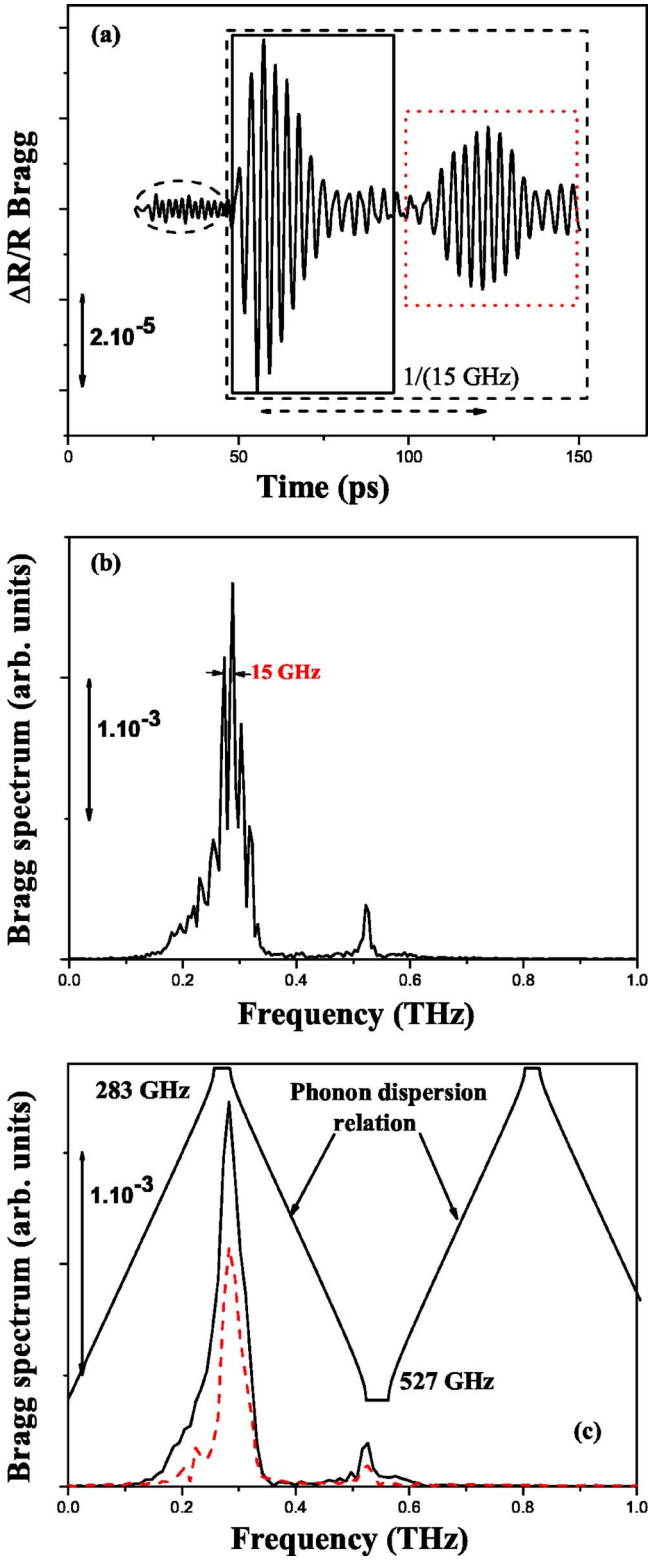


FIG. 7. (Color online) (a) Bragg reflection oscillation, (b) the corresponding direct FFT modulus of the time response in the dashed square, and (c) the FFT modulus of both acoustic bursts separately in the solid and dotted squares.

acoustic-phonon wave packet to make one round-trip in the cap layer, from which we had extracted the cap layer thickness. The frequencies of these acoustic coherent phonons,

283 and 527 GHz, correspond to the first- and second-order zone folded modes in the dispersion relation, as shown in Fig. 7(c). We note here the excellent agreement between experimentally measured frequencies and the calculated ones based on approximated formula [Eq. (13)]. The approximation is valid due to the small value of $\gamma \approx 0.026$ as we have discussed in Sec. III A. We should also note that the comparison with experimental results allows us to get the exact configuration of the SL, $A/B/A/B\ldots \equiv Si_{0.4}Ge_{0.6}/Si/Si_{0.4}Ge_{0.6}/Si/\ldots$, which means that the top SL layer is $A \equiv Si_{0.4}Ge_{0.6}$. The observed oscillations are the consequence of the temporal convolution between the coherent acoustic-phonon wave packet, generated inside both the metal film and the cap layer, and the acoustic pulse response of the SL, by analogy to the action of an electronic linear filter. In the frequency space, the temporal convolution becomes a multiplication of the coherent acoustic-phonon wave-packet spectrum and the SL acoustic transfer function, as illustrated in Fig. 6.

#### 3. Impulsive stimulated Raman scattering

A thorough analysis of the response at very early times ($t < 50$ ps) in Fig. 7(a) shows a very fast oscillation of frequency of 527 GHz, as shown in the spectrum modulus of Fig. 8(a). This is the same oscillation which persists along the entire curve as we can see in Fig. 3. We find this frequency in the spectra modulus of both acoustic bursts in Figs. 5(b) and 7(c). Since this frequency corresponds to the center of the folded mini-BZ, we deduce that the oscillation is due to direct excitation of folded phonons by residual pump light reaching the SL; this is illustrated schematically in Fig. 8(b).

This phenomenon was already observed by Bartels *et al.* in similar experimental conditions,[15,16] and it was proved that the mechanism responsible for this oscillation is a forward ISRS in which light couples to zone folded acoustic modes of the SL. These authors observed, in fact, a triplet of modes: a central mode excited via forward ISRS and two side modes excited via backward ISRS. In our case, it seems that the two side modes are hidden by coherent acoustic-phonon Bragg reflection since the acoustic pulse spectrum is extending up to 1 THz, as shown in Fig. 6. As for Brillouin oscillation, ISRS and Bragg reflection create a spatiotemporal modulation in the dielectric constant, which is responsible for the observed reflectivity change.

We should mention that the phonon frequency gap position and width are strongly dependent on the geometrical and physical properties of the studied structure. Calculations show that a small variation in the thickness or in the longitudinal-acoustic sound velocity of one of the layers $A$ or $B$ leads to a strong variation in the position and the width of the phonon frequency gaps. This high sensitivity confirms the possible identification of the SL acoustic and geometrical properties from the observed experimental data.

#### 4. Acoustic attenuation into the cap layer

One of the essential pieces of information we can get from experimental results is related to the attenuation of the

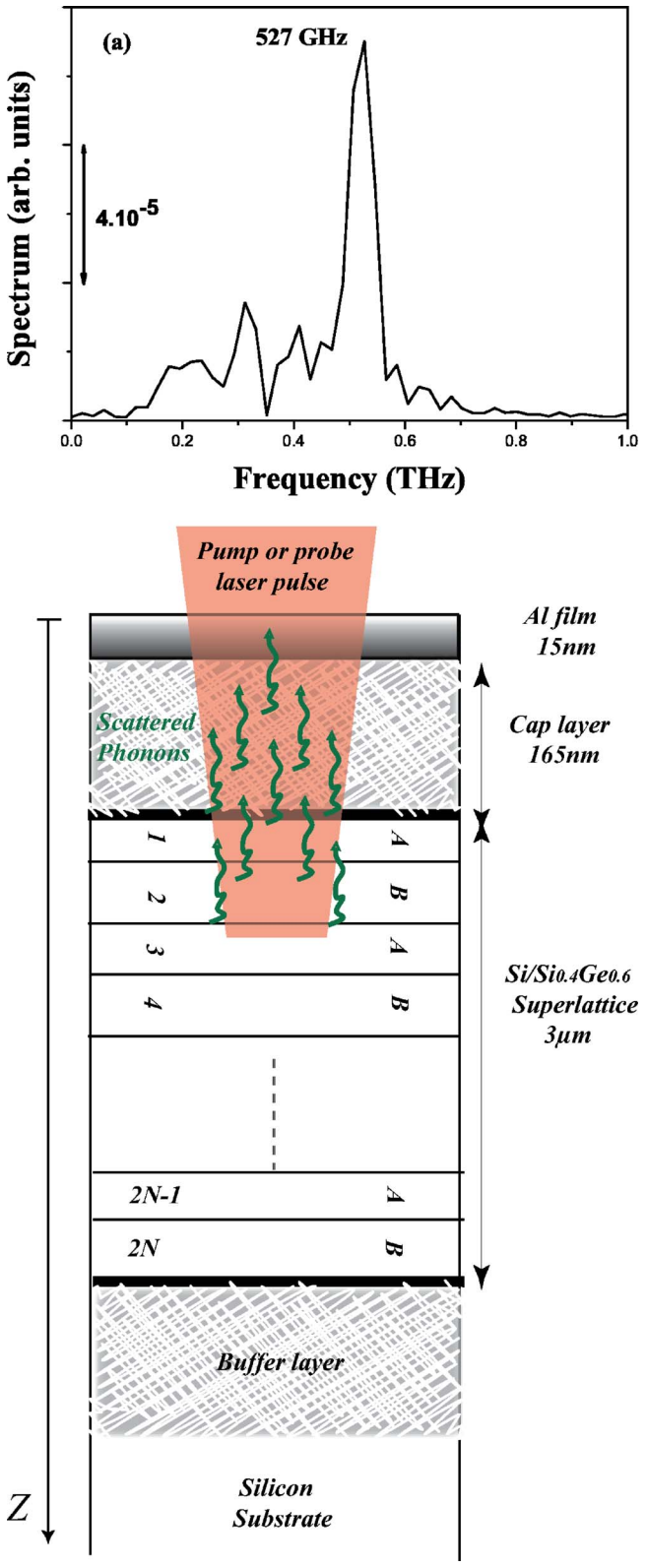


FIG. 8. (Color online) (a) FFT modulus of the signal at the beginning of the curve in Fig. 7(a) (<50 ps). (b) Schematic diagram of the studied structure illustrating absorption of the pump pulse and generation of coherent longitudinal-acoustic phonons in the superlattice.

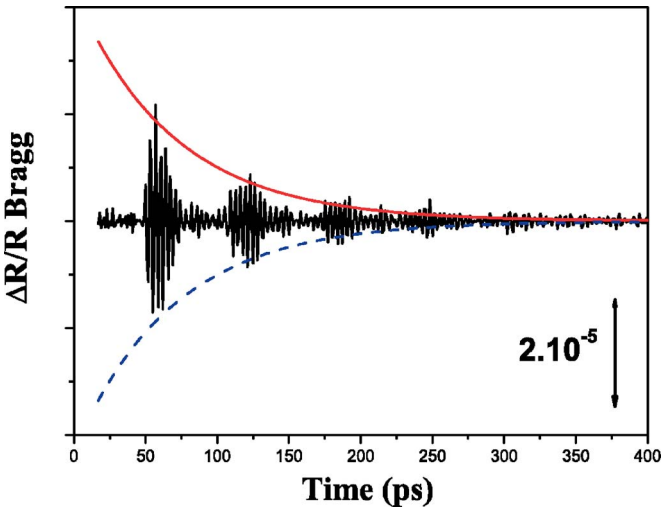


FIG. 9. (Color online) Bragg reflection oscillation after Bessel numerical filtering of the experimental result obtained in the same conditions as those in Fig. 3, but on a larger pump-probe delay. The solid and dashed exponential decays are the best fit corresponding to $A_{CL}\exp(-\alpha v_{CL}t)$ and $-A_{CL}\exp(-\alpha v_{CL}t)$, respectively, where $\alpha$ is the attenuation of coherent longitudinal-acoustic phonons in the cap layer.

coherent longitudinal-acoustic phonon wave packet within the cap layer. In Fig. 9, we show oscillations resulting from Bragg reflection after filtering the experimental results obtained in conditions the same as those in Fig. 3, but with a larger time delay between the pump and the probe. Since the Bragg reflection concerns only phonons which satisfy the Bragg condition, i.e., phonons with a defined frequency, their attenuation will be defined only at this frequency and a temporal picture will be a good description. If we assume that there is no acoustic attenuation in the Al transducer film, then it must be correct to relate two successive acoustic strains by[37]

$$\eta_2(z,t) = \eta_1(z,t) r_{CL/SL} e^{-\alpha v_{CL} t}, \tag{25}$$

where $\alpha$ is the attenuation per unit distance in the cap layer and $r_{CL/SL}$ is the acoustic reflection coefficient at the cap layer/SL interface. As shown in Fig. 2(a), for both frequency modes, the acoustic-phonon reflection rate is almost 100%; this is why we take $r_{CL/SL}=1$. The reflectivity change resulting from the acoustic strain is given by[30,37]

$$\Delta R(t) = \int_0^{d_{CL}} f(z)\,\eta(z,t)dz, \tag{26}$$

where $d_{CL}$ is the cap layer thickness and $f(z)$ is the optical sensitivity function, which determines how acoustic strain variations at different depth values below the free surface contribute to the reflectivity change. The general form of $f(z)$ is an exponentially damped oscillation with non zero phase at the free surface $z=0$. The periodicity of $f(z)$ is equal to the half wavelength of light in the material. The range of $f(z)$ is determined by the optical penetration length $\xi$ as it was calculated by Thomsen *et al.*[30] and Zhu *et al.*[37] From Eqs. (25) and (26), we obtain

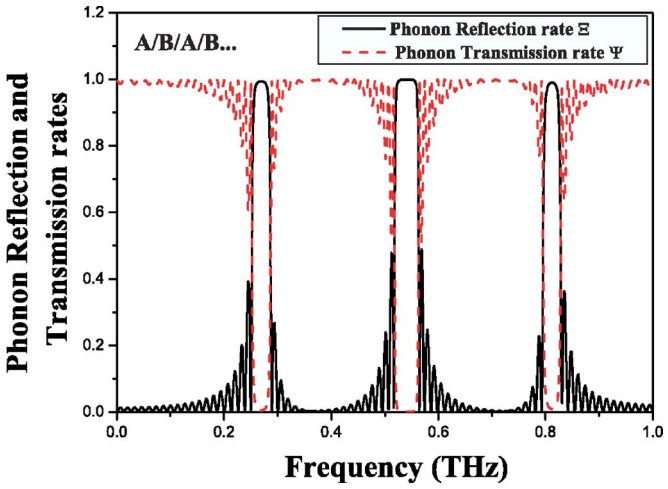


FIG. 10. (Color online) Calculated coherent longitudinal-acoustic-phonon reflection rate (solid line) and transmission rate (dashed line) in the $Si/Si_{0.4}Ge_{0.6}$ superlattice for an $A/B/A/B\ldots$ configuration with $A \equiv Si_{0.4}Ge_{0.6}$ and $B \equiv Si$.

$$\alpha = \frac{1}{2d_{CL}} \ln\left(\frac{\Delta R(t=2d_{CL}/v_{CL})}{\Delta R(t=4d_{CL}/v_{CL})}\right). \tag{27}$$

We then fitted the maxima and the minima of the acoustic bursts with $A_{CL}\exp(-\alpha v_{CL}t)$ and $-A_{CL}\exp(-\alpha v_{CL}t)$, respectively, and optimized both $A_{CL}$ and $\alpha$ to get the best fit. The result is shown in Fig. 9. With this method, we obtain an average value for the attenuation of the coherent longitudinal-acoustic-phonon wave packet, satisfying Bragg reflection condition, in the cap layer. This attenuation is $\alpha \approx 2\times 10^6\ \mathrm{m}^{-1}$, which is very high considering the small thickness of the cap layer. The acoustic echoes are damped by a factor of 2 along the 165 nm cap layer thickness. The large attenuation may be explained by the nature of the Al film which is likely to have plenty of grains.

#### *5. Reflection and transmission rates and the phonon phase-coherent length*

As mentioned in the Introduction, many authors have studied the transmission of coherent acoustic phonons in several superlattices.[2,5,8–13] In this work, we have discussed the reflection of coherent acoustic phonons. To show the similitude of the interpretations, we report both calculated reflection and transmission rates of coherent longitudinal-acoustic phonons in Fig. 10. The transmission rate of coherent longitudinal-acoustic phonons is given by

$$\Psi = \frac{\Phi_{su,a}}{\Phi_{CL,a}} = \frac{Z_{su}}{Z_{CL}} \frac{1}{|(\tau_{CL,A} T_{ac}^{SL} \tau_{A,su})_{11}|^2} = 1 - \Xi, \tag{28}$$

where $Z_{su}$ and $Z_{CL}$ are the acoustic impedances of the substrate and the cap layer, respectively.

Increasing the numbers of SL periods increases the magnitude of the reflection peaks and transmission dips as well as the number of small oscillations. These oscillations result from the interference of reflected and transmitted phonon waves, and they show nicely the reduction of the phonon phase-coherent length in the framework of the wave descrip-

tion. Since the phonon mean free path in semiconductors is in the range of 100 mm,[1] and largely exceeds the SL period, a particle motion description is no longer appropriate. The phonon phase-coherent length decreases with an increasing number of SL periods due to the incoherent scattering at interfaces. From the inverse of the frequency period of these oscillations, one could obtain information on the lifetime of the coherent phonon inside the SL.

## V. CONCLUSION

In this paper, we have presented generation and detection of coherent longitudinal-acoustic-phonon wave packet in a $Si/Si_{0.4}Ge_{0.6}$ superlattice by femtosecond laser pulses. The configuration of the structure allowed us to distinguish three different classes of coherent phonons generated by completely different mechanisms. The frequency of Brillouin oscillation is determined by the probe wavelength, while the frequencies of Bragg reflection and impulsive stimulated Raman scattering are functions of the sample geometrical and physical properties. The latter types of oscillations are a result of coherent zone folding longitudinal-acoustic phonon, and are well explained by the elastic continuum theory of acoustic modes.

## ACKNOWLEDGMENTS

The authors would like to thank Bernard Perrin for enlightening discussions and "La Région d'Aquitaine," FEDER Objectif 2, "Le Ministère de la Recherche" (CPER), DARPA, ONR, and Packard Foundation for supporting this work.

*Present address: Department of Electrical Engineering, University of California Santa Cruz, Santa Cruz, CA 95064-1077, USA. Email address: younes@soe.ucsc.edu

[1] P. Y. Yu and M. Cardona, *Fundamentals of Semiconductors: Physics and Materials Properties*, 3rd ed. (Springer, Berlin, 2001).
[2] S. Tamura, D. C. Hurley, and J. P. Wolfe, Phys. Rev. B **38**, 1427 (1988).
[3] D. G. Cahill, W. K. Ford, K. E. Goodson, G. D. Mahan, A. Majumdar, H. J. Maris, R. Merlin, and S. R. Phillpot, J. Appl. Phys. **93**, 793 (2003).
[4] P. Basséras, S. M. Gracewski, G. W. Wicks, and R. J. D. Miller, J. Appl. Phys. **75**, 2761 (1994).
[5] V. Narayanamurti, H. L. Störmer, M. A. Chin, A. C. Gossard, and W. Wiegmann, Phys. Rev. Lett. **43**, 2012 (1979).
[6] C. Colvard, R. Merlin, M. V. Klein, and A. C. Gossard, Phys. Rev. Lett. **45**, 298 (1980).
[7] C. Colvard, T. A. Gant, M. V. Klein, R. Merlin, R. Fischer, H. Morkoc, and A. C. Gossard, Phys. Rev. B **31**, 2080 (1985).
[8] O. Koblinger, J. Mebert, E. Dittrich, S. Döttinger, W. Eisenmenger, P. V. Santos, and L. Ley, Phys. Rev. B **35**, 9372 (1987).
[9] B. Jusserand, F. Alexandre, J. Dubard, and D. Paquet, Phys. Rev. B **33**, 2897 (1986).
[10] B. Jusserand, D. Paquet, F. Mollot, F. Alexandre, and G. Le Roux, Phys. Rev. B **35**, 2808 (1987).
[11] B. Jusserand and M. Cardona, in *Light Scattering in Solids V*, Topics in Applied Physics Vol. 66, edited by M. Cardona and G. Guntherodt (Springer, Berlin, 2000), Chap. 3.
[12] H. Brugger, G. Abstreiter, H. Jorke, H. J. Herzog, and E. Kasper, Phys. Rev. B **33**, 5928 (1986).
[13] D. J. Lockwood, M. W. C. Dharma-wardana, J. M. Baribeau, and D. C. Houghton, Phys. Rev. B **35**, 2243 (1987).
[14] H. T. Grahn, H. J. Maris, J. Tauc, and B. Abeles, Phys. Rev. B **38**, 6066 (1988).
[15] A. Bartels, T. Dekorsy, H. Kurz, and K. Köhler, Phys. Rev. Lett. **82**, 1044 (1999).
[16] A. Bartels, T. Dekorsy, H. Kurz, and K. Köhler, Appl. Phys. Lett. **72**, 2844 (1998).
[17] K. Mizoguchi, M. Hase, S. Nakashima, and M. Nakayama, Phys. Rev. B **60**, 8262 (1999).
[18] P. Hawker, A. J. Kent, L. J. Challis, A. Bartels, T. Dekorsy, H. Kurz, and K. Köhler, Appl. Phys. Lett. **77**, 3209 (2000).
[19] Y. K. Huang, G. W. Chern, C. K. Sun, Y. Smorchkova, S. Keller, U. Mishra, and S. P. DenBaars, Appl. Phys. Lett. **79**, 3361 (2001).
[20] H. Takeuchi, K. Mizoguchi, T. Hino, and M. Nakayama, Physica B **316–317**, 308 (2002).
[21] N. M. Stanton, R. N. Kini, A. J. Kent, and M. Henini, Phys. Rev. B **69**, 125341 (2004).
[22] R. Liu, G. Sanders, C. Stanton, C. Kim, J. Yahng, Y. Jho, K. Yee, E. Oh, and D. Kim, Phys. Rev. B **72**, 195335 (2005).
[23] R. N. Kini, A. J. Kent, N. M. Stanton, and M. Henini, Appl. Phys. Lett. **88**, 134112 (2006).
[24] A. Huynh, N. D. Lanzillotti-Kimura, B. Jusserand, B. Perrin, A. Fainstein, M. F. Pascual-Winter, E. Peronne, and A. Lemaître, Phys. Rev. Lett. **97**, 115502 (2006).
[25] G. Abstreiter, Phys. World **5**, 36 (1992).
[26] J. P. Douglas, Semicond. Sci. Technol. **19**, 75 (2004).
[27] S. M. Rytov, Akust. Zh. **2**, 71 (1956) [Sov. Phys. Acoust. **2**, 68 (1956)].
[28] C. Rossignol, B. Perrin, B. Bonello, P. Djemia, P. Moch, and H. Hurdequint, Phys. Rev. B **70**, 094102 (2004).
[29] C. Rossignol and B. Perrin, IEEE Trans. Ultrason. Ferroelectr. Freq. Control **52**, 1354 (2005).
[30] C. Thomsen, H. T. Grahn, H. J. Maris, and J. Tauc, Phys. Rev. B **34**, 4129 (1986).
[31] B. Perrin, B. Bonello, J. C. Jeannet, and E. Romatet, Prog. Nat. Sci. **S6**, 444 (1996).
[32] B. Perrin, C. Rossignol, B. Bonello, and J. C. Jeannet, Physica B **263**, 571 (1999).
[33] E. Kasper and K. Lyutovich, *Properties of Silicon Germanium and SiGe:Carbon*, EMIS Datareview Series No. 24 (INSPEC IEE, London, 2000).
[34] O. B. Wright, J. Appl. Phys. **71**, 1617 (1992).
[35] E. D. Palik, *Handbook of Optical Constants of Solids II* (Academic, London, 1991).
[36] B. Bonello, B. Perrin, E. Romatet, and J. C. Jeannet, Ultrasonics **35**, 223 (1997).
[37] T. C. Zhu, H. J. Maris, and J. Tauc, Phys. Rev. B **44**, 4281 (1991).